Experimental Verification of Dispersed Fringe Sensing as a Segment Phasing Technique Using the Keck Telescope

Fang Shi[a], Catherine M. Ohara[a], Gary Chanan[b], Mitch Troy[a], and Dave C. Redding[a]

[a]Jet Propulsion Laboratory, California Institute of Technology, Pasadena, CA 91109
[b]Department of Physics and Astronomy, University of California, Irvine, CA 92697

ABSTRACT

Dispersed Fringe Sensing (DFS) is an efficient and robust method for coarse phasing of segmented primary mirrors (from a quarter of a wavelength up to the depth of focus of a single segment, typically several tens of microns). Unlike phasing techniques currently used for ground-based segmented telescopes, DFS does not require the use of edge sensors to sense changes in the relative heights of adjacent segments; this makes it particularly well-suited to the phasing of space-borne segmented telescopes, such as the James Webb Space Telescope (JWST). In this work we validate DFS by using it to measure the pistons of the segments of one of the Keck telescopes; the results agree with those of the Shack-Hartmann based phasing scheme currently in use at Keck to within 2% over a range of initial piston errors of ±16 μm.

Keywords: segmented mirrors, wavefront sensing, dispersed fringe sensor, alignment

1. INTRODUCTION

The importance of phasing segmented mirror telescopes is generally appreciated: for a poorly phased telescope the resolution can be no greater than the diffraction limit corresponding to a segment, as opposed to the diffraction limit of the full aperture in the well-phased case.

For the Keck telescopes, the prototypes of ground-based segmented telescopes, the segment phasing problem is solved in two different ways: (1) a modified Shack-Hartmann technique [1, 2], and (2) a modified curvature sensing technique [3]. Both of these approaches rely upon the well-calibrated (in a relative sense) segment edge sensors at Keck. However, these techniques are not directly applicable to space-based segmented telescopes, such as the James Webb Space Telescope: there are no edge sensors in the baseline JWST design. Dispersed Fringe Sensing, or DFS, is intended to solve the segment phasing problem subject to this restriction.

DFS is an effective method for phasing a segmented mirror system, and has been validated extensively on several small-scale laboratory testbeds. On the JWST Wavefront Control Testbed (WCT), we demonstrated closed-loop DFS performance with an accuracy of 50 nm and a capture range of 100 μm [4, 5]. The DFS algorithm also performs well in computer simulations of the JWST 18-hexagon design, the Developmental Comparative Active Telescope Testbed (DCATT), and the double-pass JWST optical testing system at Plum Brook. In this paper, we use the Keck telescope as a test bed, and compare DFS directly to the Shack-Hartmann based phasing scheme which has been successfully used for the past decade at Keck.

This work is organized as follows. In Section 2, we present the theory of DFS in the context of applications to segmented mirrors. In Section 3, we describe the Keck telescopes, the Keck Phasing Camera System [6] (PCS), and the modifications to the PCS hardware used for the current tests. In Sections 4, we describe the experimental procedure and data analysis, respectively. In Sections 5 and 6, we describe our results and present our conclusions.

2. DISPERSED FRINGE SENSOR FOR SEGMENTED MIRROR PISTON DETECTION

The dispersed fringe sensor uses a transmissive grism as the dispersing element. The grism disperses the light from a broadband source according to its wavelength, forming a spectrum on the camera. The wavelength dispersion relation along the dispersion direction x is

$$\lambda(x) = \lambda_0 + \frac{\partial \lambda}{\partial x} \cdot x = \lambda_0 + C_0 \cdot x \tag{1}$$

where λ_0 is the central wavelength and C_0 is the linear dispersion coefficient, which depends on the characteristics of the grism. An approximate but general derivation of the basic equation has shown that intensity that governs the dispersed fringe has the form of [8],

$$I(x,y) = I_0\left[1+\gamma\cos\left(\frac{2\pi}{\lambda(x)}\delta+\phi_0(y)\right)\right] \tag{2}$$

where $I(x,y)$ is the dispersed fringe intensity along the dispersion coordinate x, δ is the optical path difference (OPD) caused by the relative piston between the segments, γ is the fringe visibility, and ϕ_0 is a phase constant that depends on where the DFS fringe is extracted. Qualitatively, periodic bright or dark bands occur in the fringe pattern along the dispersed spectrum at wavelength which satisfy (respectively) the constructive interference condition $[2\pi\delta/\lambda(x) + \phi(y)] = 2n\pi$, or destructive condition $[2\pi\delta/\lambda(x) + \phi(y)] = (2n+1)\pi$, where n is an integer. Fig. 1 illustrates how the dispersed fringe is formed. The number of fringes in the spectrum across a given bandwidth is proportional to the optical path difference, therefore provides a direct measurement of the magnitude of the piston error. Because adding π to ϕ in Eq. (2) is equivalent to changing the sign of δ, it is clear that the sign of the OPD cannot be extracted from a single row of pixels. The sign of δ can be determined, however, by an examination of the signal in neighboring rows, since these will have different values of the phase factor $\phi(y)$; we typically consider the central row and the rows immediately above and below it. Fringes in Fig. 1 graphically show the effect of the piston sign and fringe band orientation. The DFS algorithm uses least square fit to solve the four parameters in the fringe equation of Eq. (3): I_0, γ, ϕ_0, and absolute value of OPD δ from measured fringe intensities of each row. Then the values of ϕ_0 from upper and lower rows are compared to provide the information of the sign of the OPD δ.

Detailed considerations show that DFS is subject to four regions of reduced sensitivity. The first such region corresponds to near phased condition where δ is very small. Note that fringe intensity approach a constant, or lack of fringe modulation, as δ approaches to zero, where the constructive interference happens to most of the spectral wavelength. The lack of intensity modulation will cause the fringe fitting algorithm breaks down. [This problem does not show up in Fig. 2 because the modulation is still mathematically well-defined, even if it cannot practically be extracted by curve-fitting in the presence of noise]. The problem manifests itself when the edge step produces about one fringe or less across the detector. To avoid this problem in the measurements described here, we conservatively exclude from consideration edge steps with $|\delta| \leq 1$ μm (corresponding to about 1.5 fringes or less). Alternatively, the problem could be dealt with by deliberately introducing an offset of 1 μm or so for edges which produce some modulations.

The second region of reduced sensitivity of DFS is where the piston error is too large. At large $|\delta|$ the fringe modulation becomes dense (denser at blue end) and eventually exceeds the spectral resolution of DFS. The maximum detectable piston depends on the spectral resolution, which is defined by the imaging system sampling, dispersion of the grism and the spectral range. For system that has spectral resolution of R_0 and is critically sampled at λ_0, and working on the spectral range with blue end wavelength λ_B, the maximum wavefront piston error δ_{max} is about,

$$\delta_{\max} = \left[\frac{R_0}{2}\left(\frac{\lambda_B}{\lambda_0}\right)+1\right]\cdot\lambda_B \tag{3}$$

As δ increases beyond the δ_{max} the fringe modulation dramatically decreases because of the fringe becomes under resolved. However, unlike the situation when the δ approaching to zero, the DFS algorithm does not break down immediately because the fitting at the longer wavelength end can still provide valid solution [5]. In this experiment the algorithm was not limited by the large piston.

The other two regions, which occur only when the inter-segment edge is not parallel to the dispersion direction. For hexagonal segments there are edges at angles of not only 0°, but also ±60° with respect to the dispersion direction. For these cases there are additional regions of reduced sensitivity and it is best pursued numerically. Since the sign of segment piston is relative between segments we use the following conventions (see Fig. 3), which are determined by the orientation of the edge. Edge 7 (at an orientation of 0°) is positive if Segment B lies above D, Edge 5 (at an orientation of 60°) is positive if Segment C lies above A, and Edge 6 (at an orientation of -60°) is positive if Segment B lies above C. Fig. 1 illustrates the formation of a fringe for three different edge angles. For each edge angle a pair of numerically simulated fringes is shown. In the lower one of each pair, the fringe is sparsely sampled at a number of discrete wavelengths in order to provide some insight into how the fringe is built up from a continuous spectrum of wavelengths. In the upper fringe of each pair, the wavelength sampling is dense and the individual diffraction patterns are blurred together to form a dispersed fringe. Note that the orientation of the diffraction pattern for a positive edge step at an edge angle of -60° (top trace in Fig. 1) is such that it tends to fill in the dark bands in the fringe and significantly reduce the fringe visibility. Thus an edge at +60° forms a relatively low modulation fringe from the positive edge step and an edge at -60° forms a similarly low modulation fringe from the negative edge step. Fringe visibilities for all three orientations as determined from simulations are presented in Fig. 2. This ±60° effect (which is confirmed in the experiments described below) represents a complication for DFS in the current implementation. It can be addressed, for example, by splitting the beam, and using different grisms for different orientations, or by using a more complicated mask geometry, but we do not pursue such remedies here.

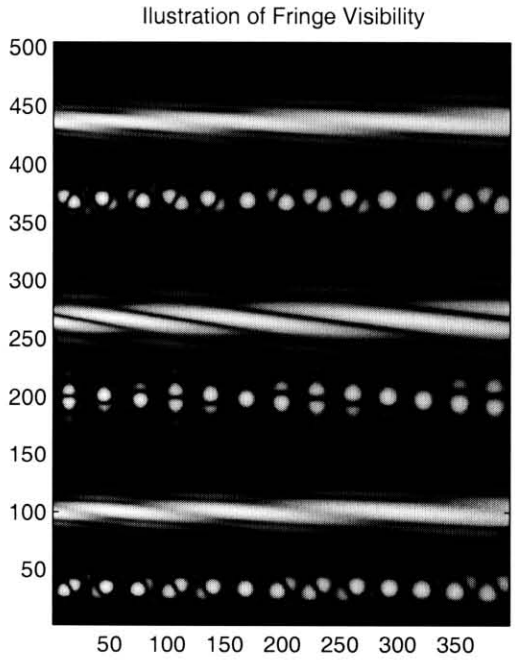

Figure 1. Simulated fringe formation for the three different edge orientations for an edge height of $+4 μm. The display is logarithmically stretched to accentuate the diffraction effects. From bottom to top, the three pairs of fringes correspond to edge orientations of -60°, and +60°. The lower of each pair uses discrete sampling to illustrate the build-up of the fringe. The upper of each pair shows the full dispersed fringe that results from dense wavelength sampling. Note that for edges oriented at +60° and positive edge heights, the individual diffraction patterns are oriented so that they tend to fill in the dark bands on each fringe and so reduce the visibility. A similar effect occurs for edges oriented at -60° and negative edge heights.

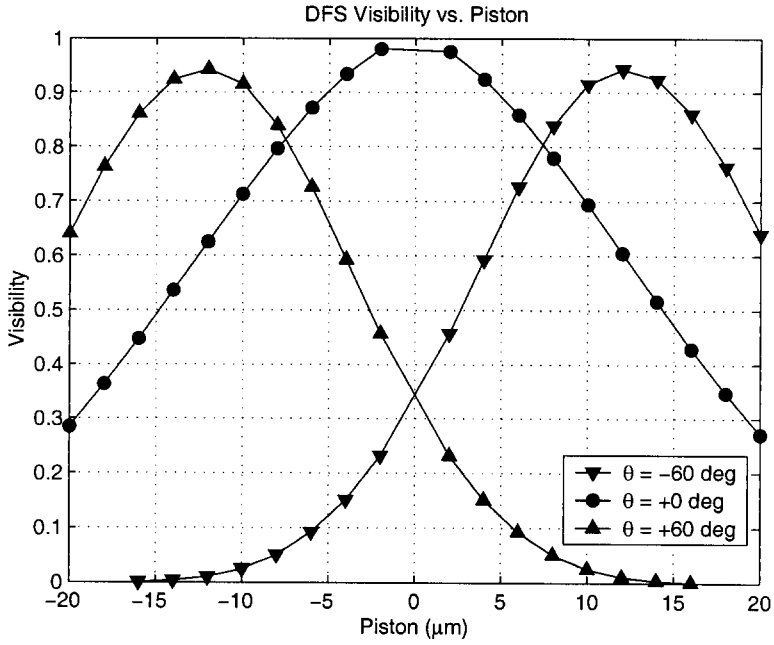

Figure 2. Theoretical fringe visibility curves for the three different edge orientations.

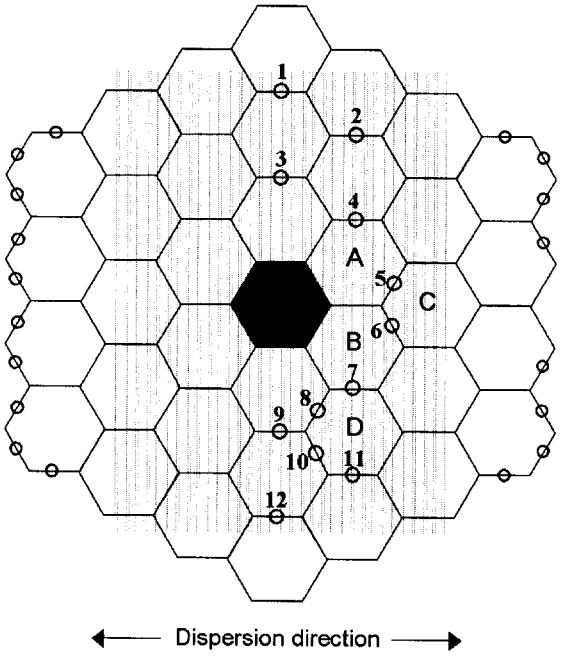

Figure 3. Geometry of the primary mirror of the Keck telescopes, showing the 12 circular subapertures which sample the inter-segment edges in the DFS mask. Each segment is 0.90 meters on a side. The subapertures are 12 cm in diameter. The 18 peripheral subapertures are used for pupil registration. The location of the grism with respect to the subapertures is indicated by the gray rectangle.

3. HARDWARE DESCRIPTION

3.1. The Keck Telescope

Except for instrumentation, the two Keck telescopes [7] are virtually identical. The experiments described in this work were carried out at the Keck 2 telescope. The primary mirror of each Keck telescope consists of 36 hexagonal segments, each 90 cm on a side, and an Active Control System (ACS) of sensors and actuators which freezes the relative positions of the segments, stabilizing the structure against gravity and thermal effects. The ACS can also be used to introduce specific misalignments into the primary mirror in a controlled way, as was done in the experiments described here. Note that there is no absolute optical reference in the ACS; the ACS stabilizes the sensor readings at their desired values once these are determined, but these desired values must be determined by independent optical means. The Phasing Camera System, described below, was developed for this latter purpose.

3.2. Phasing Camera System

The Keck Phasing Camera System [6], or PCS, is a Shack-Hartmann type wavefront sensor, which is permanently mounted at one of the Cassegrain focal stations of each of the Keck telescopes. The PCS optics re-images the primary mirror at a magnification of 1/200 in the collimated beam. A mask at the position of the re-imaged primary defines circular subapertures of diameter d = 12 cm (referred to the primary) at the center of each of the inter-segment edges. Immediately following the mask, in normal operations, is an array of prisms. The mask and prisms form an integral subassembly, which can be reproducibly inserted into the collimated beam with a wheel and detent mechanism. The prisms, in combination with a single objective lens, map the collimated sub-beams onto a 1024 x 1024 pixel CCD in a pattern that replicates the geometry of the primary mirror. The size of the subapertures is chosen to be significantly smaller than the atmospheric coherence diameter r_0, of about 20 cm at a wavelength of 0.5 μm, so that atmospheric turbulence represents only a small perturbation to the overall wavefront.

The mask-pupil registration is critical to this modified Shack-Hartmann scheme, as the subapertures must be accurately aligned with respect to the inter-segment edges. We measure this registration (and monitor it with every CCD exposure) by means of additional peripheral subapertures at outer segment edges. Typical registration accuracy of the mask is ±0.03° of rotation, and ±1.2 mm of translation in each dimension (referred to the primary mirror). With a single exposure on a moderately bright star (typically 4th to 7th magnitude), we obtain a well-separated sub-image or diffraction pattern on the detector for each unobscured inter-segment edge. The diffraction patterns are of order λ/d or 1 arcsecond in width. The image scale on the detector is 6.50 pixels per arcsecond.

3.3. DFS Implementation into PCS

For the DFS measurements performed here, we fabricated an alternative sub-assembly with a mask followed by a single lens and a grism, with the single lens replacing the usual prism array. The dispersion direction of the grism was aligned with the rows of the CCD. To optimize the maximum detectable piston error over the PCS field-of-view and wavelength operating range, we selected a grism with 150 grooves/mm and a central wavelength of 650 nm.

The DFS mask was similar to the normal PCS mask, except that only 12 of the subapertures were left clear so that the dispersed fringes from the other subapertures in the row would not run into one another (Fig. 3). To investigate the effects of fringe crowding, several of the subapertures were spaced conservatively far apart from one another in the vertical direction (#1-6 and #12 in Fig. 3), while others were spaced closer together (#7-11). Selected subapertures include segment edges at 0°, +60°, and -60° to enable us to investigate the dependence of the fringe visibility on the sign of the edge step. Light from 18 of the peripheral subapertures did not pass through the grism, but did pass through the mask, so that these peripheral spots could be used for mask-pupil registration.

4. EXPERIMENT PROCEDURES AND DATA PROCESSING AND ANALYSIS

The Keck telescopes are normally phased using the broadband phasing procedure [6], which has a capture range of ±30 μm and an accuracy of 30 nm. For the most accurate work, the phasing is refined using the narrowband algorithm [2], which has an accuracy of 10 nm, but a capture range of only about 200 nm. For the experiments conducted here, the telescope segments were aligned in tip/tilt and then accurately phased using the broadband algorithm followed by the

narrowband algorithm. We then used the telescope ACS to produce a variety of primary mirror configurations consisting of pure segment piston errors. Both random and non-random primary mirror configurations were used. Fig. 4 shows the distribution of all the edge heights (0.5 to 16 μm) that were studied in this experiment. In the non-random configurations, all non-zero edge heights had the same value. For the particular DFS mask used in this work, subaperture #8 had an edge height of zero in the non-random configurations; these cases were excluded from the analysis in Section 5.

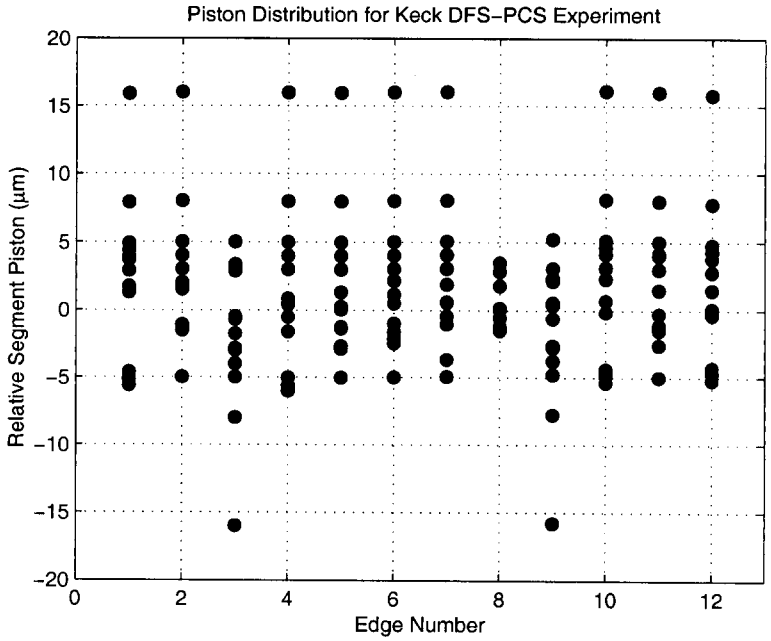

Figure 4. Edge height distribution for all experimental trials.

Because there was some uncertainty about the absolute accuracy of the ACS, the edge heights in these misphased configurations were measured directly using the PCS single-wavelength narrowband algorithm (wavelength λ = 852 nm). In most cases, these edge heights exceeded the formal capture range of this algorithm, but the correct phase was "unwrapped" by using the fact that the edge height was approximately known from the ACS piston command.

As shown in Fig. 5, each DFS image contains dispersed fringes from the 12 inter-segment subapertures as well as 18 undispersed peripheral spots for pupil mask registration. The mean background level, computed from the dark regions near the upper and lower part of each image, was fitted and subtracted out as the dark background. The centroid positions of the peripheral spots were used to shift and re-center each image.

The DFS wavelength dispersion on the detector was calibrated using three narrow-band filters centered at 619, 651, and 891 nm (FWHM of 10 nm). Because of chromatic aberration, the wavelength calibration was computed separately for each of the 12 subapertures. A maximum 2.4% variation in the dispersion was observed, depending on the subaperture position from the center. More details on this will be discussed in the next section.

The DFS signals contain spectral information from both the star and the instrument, as well as the modulation from the piston error. The unwanted spectral features of the star and instrument were removed by dividing out a reference fringe that contains no piston modulation. The reference fringe image was acquired by translating the pupil in x and y (using a pupil steering mechanism inside PCS), such that the subapertures on the mask coincided with the segment centers (where the piston error is zero) rather than the inter-segment edges. After the reference spectrum was removed from the raw DFS signal, the processed signal contained only the modulation from the piston error. As described in Section 2, the intensity signals were then fit to the fringe equation using a least-squares method to detect the inter-segment pistons.

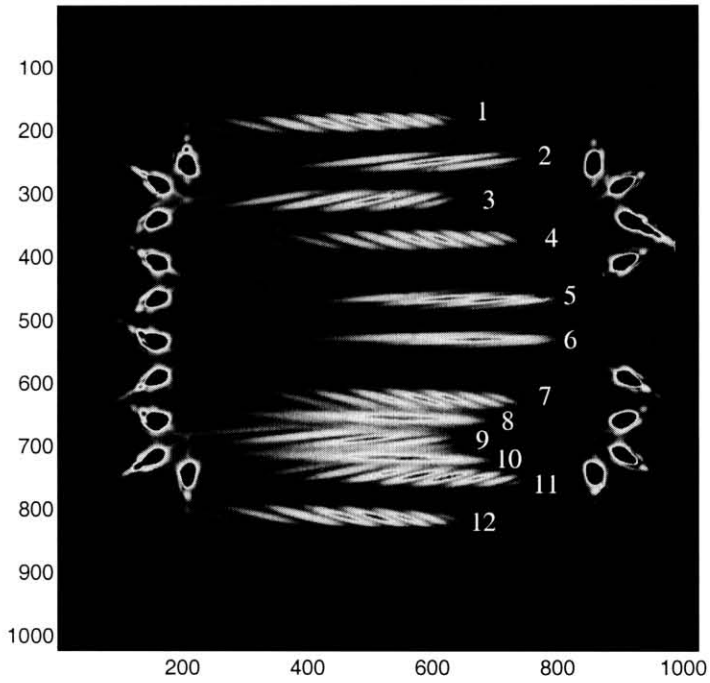

Figure 5. A sample DFS image showing 12 dispersed fringes from the inter-segment edges, and 18 peripheral spots (undispersed) used for pupil registration. The display has been stretched to accentuate the fringes.

5. RESULTS AND DICUSSIONS

Fig. 6 shows the processed signals and the corresponding best-fit theoretical curves for a typical edge. For this edge (Number 3) the orientation is 0°, so the fringes are visible for both positive and negative edge steps. As predicted, the visibility decreases with increasing edge step. The experimental visibilities are lower than the theoretical curve in Fig. 2, probably because of aberrations in the optical system and atmospheric seeing.

The fitting algorithm monitors the best-fit amplitude and visibility to determine the quality of the piston solution. If the fitted amplitude is unreasonably large or the visibility too small, the algorithm will ignore the measurement. An example case is shown in the upper left plot in Fig. 6, where the piston is at zero. This prevents the algorithm from mistakenly fitting to the noise in the fringe in cases where the fringe visibility is very low compared to the noise level, such as when the segments are nearly phased or in the presence of large segment aberrations [4, 5].

The summary plot including all 12 subapertures is shown in Fig. 7, which compares the DFS detected edge heights to the corresponding PCS measurements. The DFS and PCS results agree to within 2% over a range of piston errors from 1 to 16 μm. Edge height measurements for edges that were nearly phased ($|d| \leq$ μm) or had low fringe visibilities as a result of the ±60° effect (see Section 2) were eliminated from consideration.

We also analyze those edges oriented at ±60° which fell into the two regions of reduced sensitivity specific to their orientation. Fig. 8 depicts six DFS signals with similar absolute edge heights, but with different signs and edge orientations. As expected, when the edge was oriented at 60°, the fringe was washed-out if the edge height was +5 μm, and similarly for edges at -60° with a height of –5 μm. Further considerations on the sensitivity of the fringe visibility to the sign of the piston error for non-parallel edge orientations have been presented elsewhere [5].

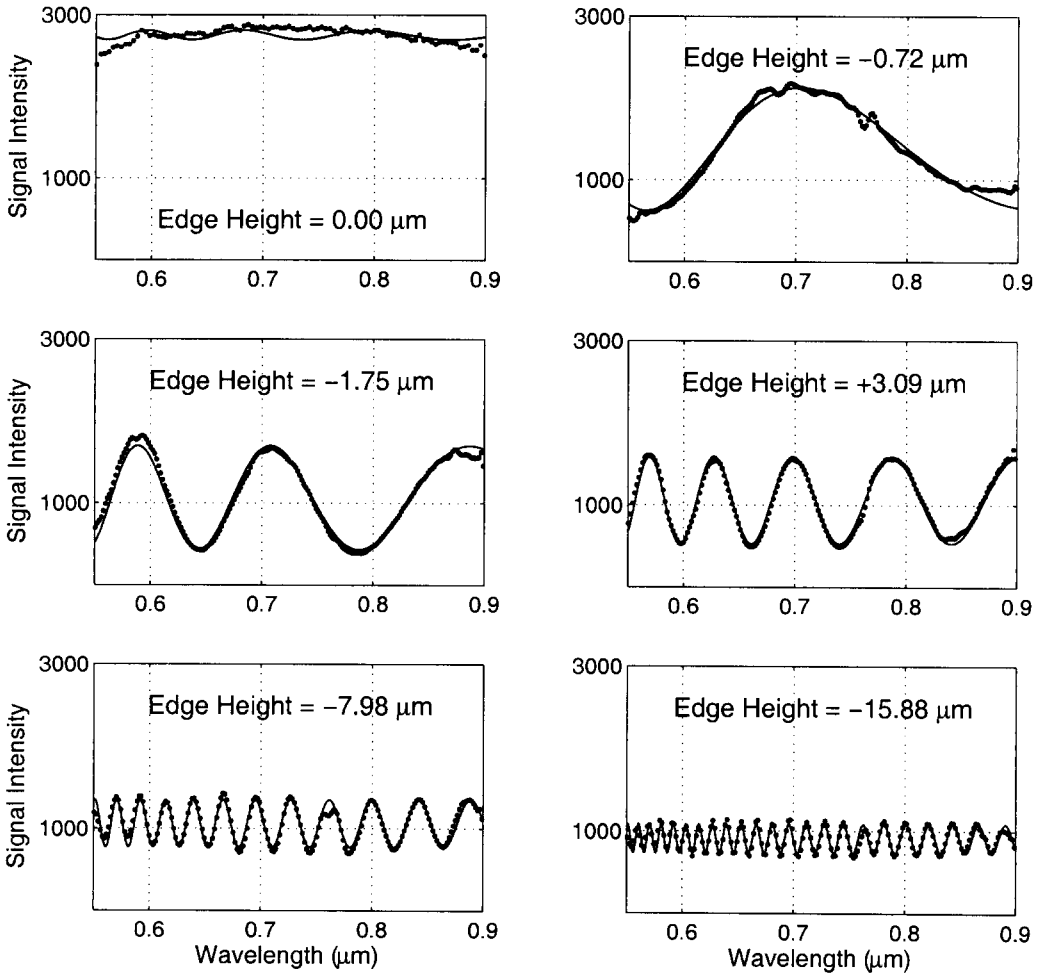

Figure 6. Sample DFS signal intensities for Edge #3 (at an orientation of 0°), depicting a range of piston values. The corresponding fits to Eq. xxx are also shown. The upper left plot is an example of two segments that are nearly phased - such results are discarded by the fitting algorithm because the calculated fringe contrast is too low. Also, as the absolute piston value increases, the fringe visibility decreases as a result of the limited spectral resolution; this defines the DFS capture range.

As described in Section 3, the subapertures in the DFS mask were selected to investigate the effect of fringe crowding on the piston detection error. Our results indicate there is no noticeable difference in the detection between fringes that are well separated and fringes that are closely spaced. This is because the fringes are well sampled (~ 6.5 pixels across λ/d), while the DFS signal requires only three adjacent rows of pixels extracted from the center of the fringe.

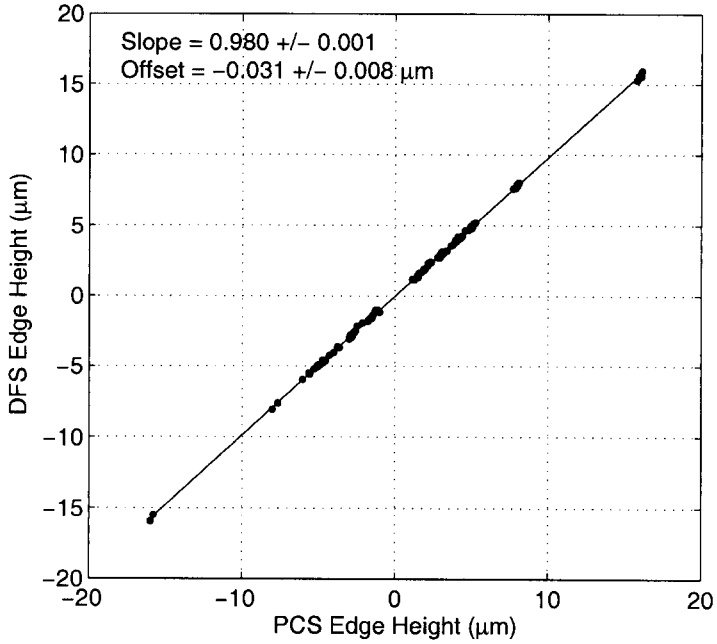

Figure 7. DFS measurements compared to PCS measurements, excluding the data points corresponding to the three regions of reduced sensitivity, as described in the text. The best straight-line fit yields a slope that is close to unity (0.980 ± 0.001) and a systematic offset of 30 ± 8 nm.

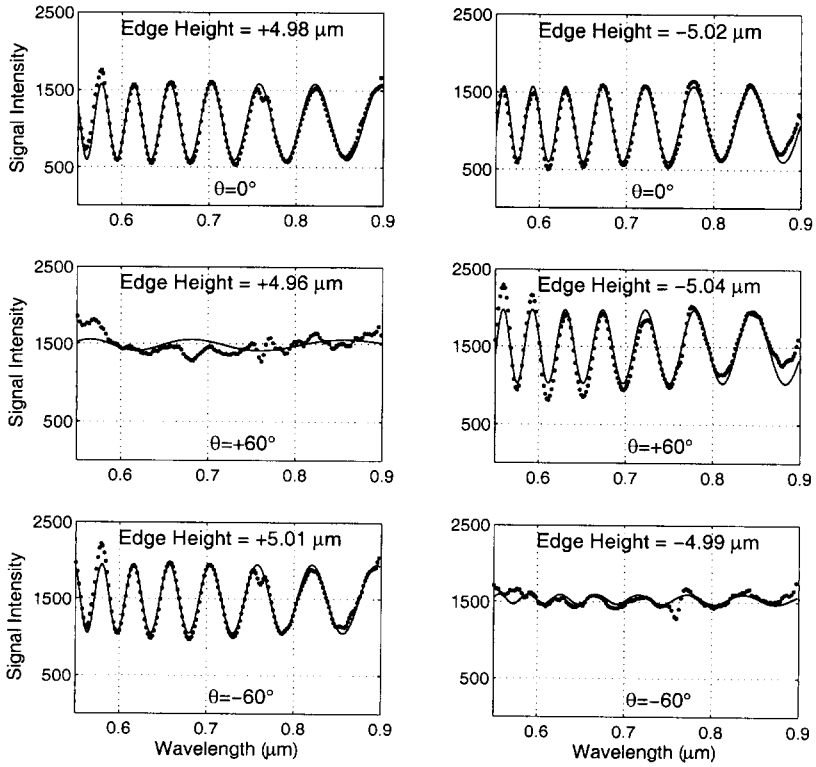

Figure 8. Comparison of the fringe visibility for positive edge heights (left column) and negative edge heights (right column), for various edge orientations. For edge orientations of ±60° (but not for 0°), the fringe visibility is sensitive to the sign of the edge height, as shown in the middle row (60° edge orientation) and bottom row -60° edge orientation).

The DFS detection errors (DFS minus PCS measurements) are summarized in Table 1. An examination of the DFS versus PCS differences reveals a systematic trend in the residual error that is linearly proportional to the initial segment piston. The systematic error was observed in all 12 edges, with a mean value of 20 nm/μm or 2.0% (Fig. 9). As discussed below the systematic trend is mainly due to the errors in the DFS's wavelength dispersion calibrations. Since wavelength calibrations are carried independently for each subaperture the systematic trends are different from edge to edge. After the best-fit straight line was removed for each subaperture, the detection error was significantly reduced (see the last column in Table 1). The total uncorrected rms error is 142 nm while the total corrected error is 59 nm.

We have considered that the DFS-PCS discrepancy might originate on the PCS measurement, but this does not seem to be the case. To demonstrate this, we compared the PCS measurements to those inferred from the ACS commands. Although the Keck ACS has never been calibrated against PCS (so that the ACS commands and PCS measurements are in fact independent), the systematic difference between PCS and ACS was found to be 0.2% ± 0.1%. In view of this agreement, it is reasonable to attribute virtually the entire DFS-PCS systematic difference to DFS.

Detailed study and simulation has shown that this systematic discrepancy between DFS and PCS is due to a systematic error in the DFS wavelength calibration. DFS algorithm relies on the wavelength calibration to relate the fringe pixel positions to corresponding wavelengths. Therefore the accuracy of the fitted solutions to the fringe equation, including OPD δ, from the fringe intensity is very much relied upon the accuracy of wavelength calibration. The wavelength calibration error will cause the piston detection error which is linearly proportional to the piston value – the systematic trend we saw in the experiment results. The simulation shows that as the wavelength dispersion error increase the systematic trend slope increase (Figure 10).

In the experiment the wavelength calibration was down by inserting three narrow band filters. The centroid positions of these narrow band images calibrate the wavelength-pixel position for spectra from each of the 12 subapertures. We found that the major contribution of the wavelength dispersion calibration error is the chromatic aberration in the PCS optics (which are designed to minimize chromatic effects only upstream from the exit pupil). From the narrow band PCS image we calculate that lateral color (image magnification difference between tow colors normalized by the mean magnification) over the spectral range in the experiment (0.55 – 0.9 μm) is 0.035. From the plot in Fig. 10 the systematic trend slope caused by the lateral color will be –0.018 μm/μm. This value is a good match to the mean systematic trend slope (2%) we observed in our data. Another contribution in wavelength dispersion calibration, although believed to be minor, is the centroid errors in the process of narrow band image. Due to the small residual inter-segment piston after the telescope was phased by PCS the subaperture PSFs in the narrow band images are non-symmetric and cause the centroid error. Simulations has shown that the residual inter-segment piston can cause the centroid error as large as 2 pixels, which corresponding to 0.5% of wavelength calibration error.

Table 1. Summary of DFS inter-segment height measurements. Errors are with respect to PCS: Uncorrected final RMS piston errors are calculated without removing the systematic trend; corrected final RMS piston errors are calculated with systematic trend removed.

Edge No.	No. Measurements	Systematic Trend (μm/μm)	Final RMS Piston Error Uncorrected (μm)	Final RMS Piston Error Corrected (μm)
1	16	0.017	0.141	0.031
2	16	0.015	0.116	0.067
3	14	0.018	0.128	0.048
4	11	0.021	0.154	0.030
5	6	0.029	0.141	0.090
6	12	0.016	0.158	0.117
7	12	0.013	0.183	0.056
8	2	0.00*	0.113	0.00*
9	13	0.008	0.100	0.063
10	7	0.024	0.079	0.038
11	15	0.022	0.158	0.037
12	14	0.014	0.164	0.070

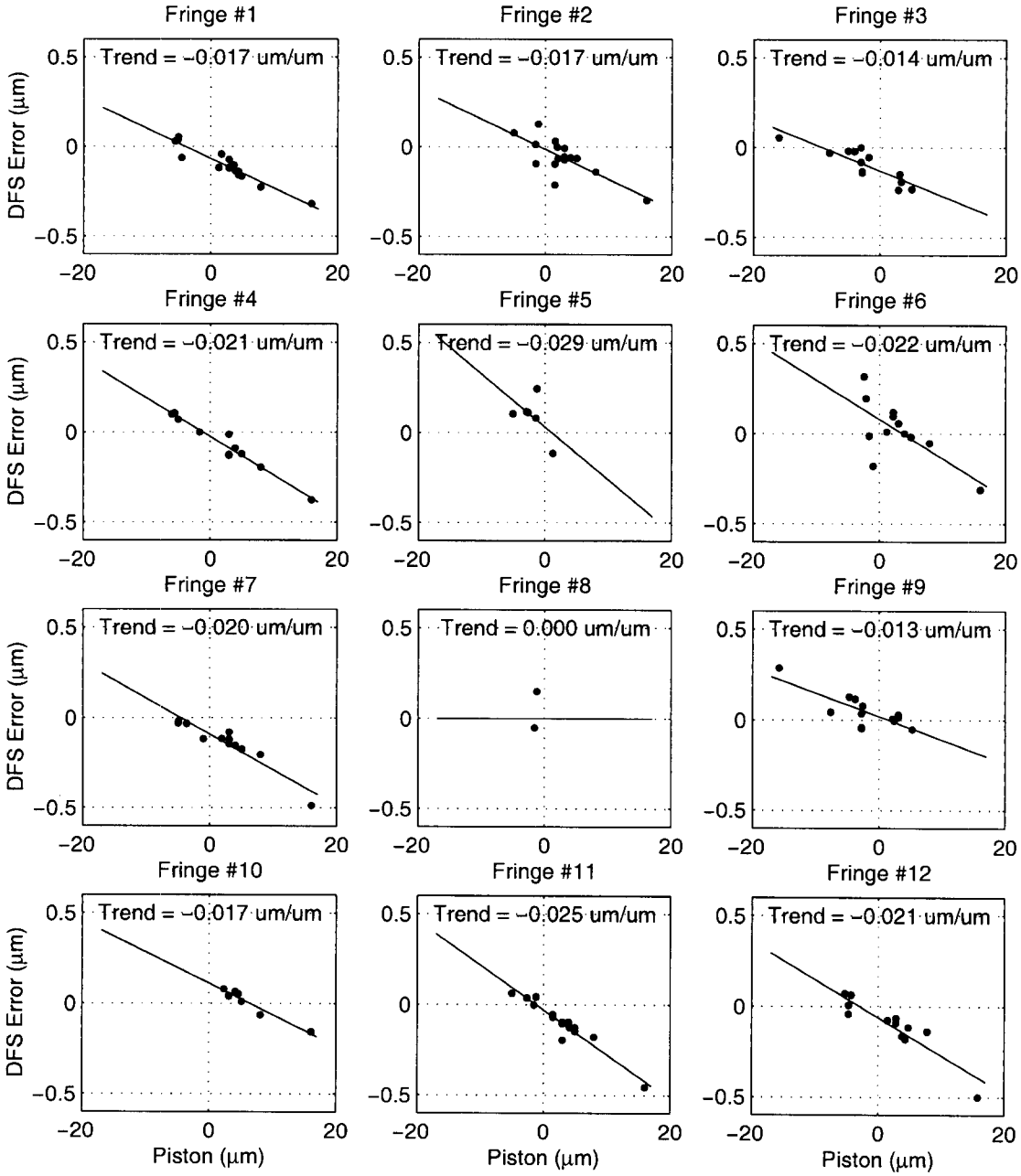

Figure 9. DFS detection error (relative to PCS) versus edge height, excluding the data points corresponding to the three regions of reduced sensitivity. The best straight-line fit is also plotted with systematic trend slope indicated.

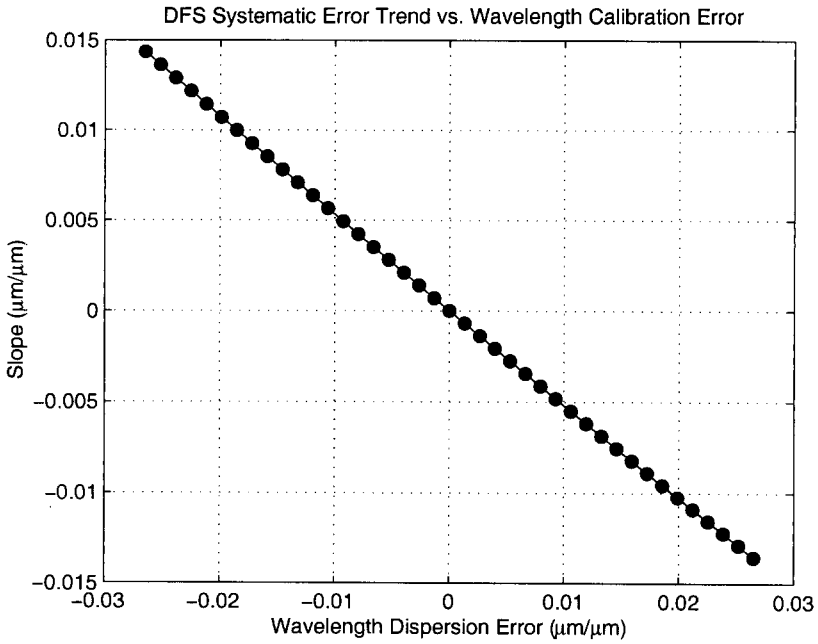

Figure 10. Keck simulation which shows that the DFS piston detection error systematic slope (the ratio of DFS error over the piston) is proportional to the wavelength dispersion calibration error (the percentage changes of wavelength dispersion).

6. CONCLUSIONS AND FUTURE WORK

In this experiment, we used DFS to accurately measure segment piston errors ranging from approximately one wave (~ 1 μm) up to 16 μm. For DFS only a single broadband measurement was required to measure multiple edges in parallel. As benchmarked against PCS, DFS is highly accurate in measuring segment pistons, with an rms error (averaged over all 12 subapertures) of about 142 nm. With improved calibration procedures, the accuracy would be 59 nm.

In summary, the high level of agreement between the DFS and PCS results presented here provides strong validation of the DFS algorithm under realistic conditions for a large segmented-mirror telescope. These observations highlight both the high level of efficiency of DFS and the need for accurate wavelength calibration.

With the success in the Keck DFS experiment we are now considering another DFS experiment using PCS on the Keck Telescope. In this experiment two new subaperture masks and DFS assemblies will be used to mimic the geometry of JWST's Dispersed Hartmann Sensors (DHS), a DFS type designed sensor for JWST's baseline segment coarse phasing. Besides measuring the edge height we also will test the wavefront reconstruction algorithm from the segment edge measurements and perform a closed-loop control on the Keck Telescope.

ACKNOWLEDGEMENTS

This research was carried out at the Jet Propulsion Laboratory, California Institute of Technology, under a contract with the National Aeronautics and Space Administration (NASA); at the University of California at Irvine, supported in part by the National Science Foundation Science and Technology Center for Adaptive Optics, managed by the University of California at Santa Cruz under cooperative agreement AST-9876783; and at the Keck Observatory. We are grateful to the Keck Observatory for making engineering time available to us for the purpose of these experiments, and to Barbara Schaefer for assistance with the observations.

REFERENCES

[1] G. A. Chanan, M. Troy, F. G. Dekens, S. Michaels, J. Nelson, T. Mast, and D. Kirkman, "Phasing the Mirror Segments of the Keck Telescopes: the Broadband Phasing Algorithm," Applied Optics **37**, 140 - 155 (1998).

[2] G. A. Chanan, C. Ohara, and M. Troy, "Phasing the Mirror Segments of the Keck Telescopes II: The Narrow-band Phasing Algorithm," Applied Optics **39**, 4706 - 4714 (2000).

[3] G. Chanan, M. Troy, and E. Sirko, "Phase Discontinuity Sensing: A Method for Phasing Segmented Mirrors in the Infrared," Applied Optics **38**, 704 - 713 (1999).

[4] F. Shi, D. C. Redding, C. W. Bowers, A. E. Lowman, S. A. Basinger, T. A. Norton, P. Petrone III, P. S. Davila, M. E. Wilson, and R. A. Boucarut, "DCATT dispersed fringe sensor: modeling and experimenting with the transmissive phase plates," in *UV, Optical, and IR Space Telescopes and Instruments*, J. B. Breckinridge and P. Jakobsen, eds., Proc. SPIE **4013**, 757 - 762 (2000).

[5] F. Shi, D. C. Redding, A. E. Lowman, C. W. Bowers, L. A. Burns, P. Petrone III, C. M. Ohara, and S. A. Basinger, "Segmented mirror coarse phasing with a dispersed fringe sensor: experiments on NGST's Wavefront Control Testbed," in *IR Space Telescopes and Instruments*, J. C. Mather, ed., Proc. SPIE **4850**, 318 - 328 (2002).

[6] G. A. Chanan, "Design of the Keck Observatory Alignment Camera," in *Precision Instrument Design*, T. C. Bristow and A. E. Hatheway, eds., Proc. SPIE **1036**, 59 - 70 (1988).

[7] J. E. Nelson, T. S. Mast, and S. M. Faber, "The Design of the Keck Observatory and Telescope," Keck Observatory Report No. 90, W.M. Keck Observatory, Kamuela HI (1985).

[8] F. Shi, G. A. Chanan, C. Ohara, M. Troy, and D. C. Redding, "Experimental verification of Dispersed Fringe Sensing as a Segment Phasing Technique Using the Keck Telescope," to be publish in Applied Optics (2004).